Spores and extracellular matrix components impart molecular order in *Bacillus subtilis* biofilms.

David N Azulay[1#], Oliver Späker[2#], Mnar Ghrayeb[1], Michaela Wilsch-Bräuninger[3], Ernesto Scoppola[2], Manfred Burghammer[4], Ivo Zizak[5], Luca Bertinetti[6], Yael Politi[6]* and Liraz Chai[1,8]*

1 Institute of Chemistry, the Hebrew University of Jerusalem, Edmond J. Safra Campus, Jerusalem 91904, Israel
2 Department of Biomaterials, Max Planck Institute of Colloids and Interfaces, 14476 Potsdam, Germany
3 Max Planck Institute of Molecular Cell Biology and Genetics, 1307 Dresden, Germany
4 European Synchrotron Radiation Facility (ESRF)71, avenue des Martyrs, CS 40220, Grenoble Cedex 9 38043, France
5 Helmholtz-Zentrum Berlin, Department Structure and Dynamics of Energy Materials, Berlin, Germany
6 B CUBE - Center for Molecular Bioengineering, Technische Universität Dresden, Dresden, Germany
7 The Center for Nanoscience and Nanotechnology, The Hebrew University of Jerusalem, Edmond J. Safra Campus, Jerusalem 91904, Israel

# equal contribution

* *To whom correspondence should be addressed: Dr. Liraz Chai, Institute of Chemistry, The Hebrew University of Jerusalem, Edmond J. Safra Campus, Jerusalem 91904, Israel. Telephone: +972-2-6585303, Fax. +972-2-5660425. Email. Liraz.chai@mail.huji.ac.il; Dr. Yael Politi, B CUBE - Center for Molecular Bioengineering, Technische Universität Dresden, 01307 Dresden, Germany. Email. yael.politi@tu-dresden.de*

Abstract

Biofilms are surface-associated soft microbial communities, which may be either detrimental or beneficial to their hosting environment. They develop from single cells into mature colonies, that are composed of cells and sometimes (in *Firmicutes* phylum) spores, held together by an extracellular matrix (ECM) of secreted biomolecular components. Biofilm development is a dynamic process, during which cells organize into subgroups, creating functionally distinct regions in space. Specific examples of functional-spatial division in *Bacillus subtilis* biofilms include matrix and spore formation as well as water channels that form beneath wrinkles. An interesting question arising is whether the division of labor in biofilms is also reflected in the molecular-level order across whole biofilms. Using combined X-ray diffraction (XRD)/X-ray fluorescence (XRF), we studied the molecular order in intact biofilms across multiple length scales. We discovered that biofilms display a distinct spatio-temporal XRD signature that depends on highly ordered structures in spores and on cross β sheet structures in matrix components. Spore signal is found especially enhanced with water molecules and metal-ions signals along macroscopic wrinkles, known to act as water channels. Demonstrating *in situ* the link between molecular structures, metal ions distribution and division of labor across whole biofilms in time and space, this study provides new pivotal insight to the understanding biofilm development.

Introduction

Biofilms are soft microbial communities that form on surfaces and at interfaces(*1, 2*). Bacterial biofilms are composed of vegetative cells that are embedded in a network of secreted polysaccharides, proteins and nucleic acids, termed the extracellular matrix (ECM)(*3*). The ECM network provides biofilms with diverse essential properties (*4*), endowing mechanical stability (*5, 6*), regulating spreading (*7*) and osmotic pressure (*8*), water and mineral uptake(*9*), providing a hydrophobic shield (*10, 11*), affecting the precipitation of minerals such as calcium carbonate (*12, 13*), and increasing the resistance of the biofilm cells to antibiotic activity (*4, 14*). Biofilms of bacterial cells from the *Firmicute* phylum, such as *Bacilli* and *Clostridia* can also form spores (*15*), which are metabolically dormant cells that store their genome in a partially dehydrated core. The spore core is surrounded by a protective coat, composed of highly ordered layers of ~ 70 proteins and glycoproteins (*16-18*). Biofilm spores often reside in aerial structures, projecting from the biofilm's surface, to facilitate their dispersal (*19*) (*20*).

The realization that nomadic bacterial cells may adopt a communal form of life (*21, 22*) greatly stimulated biofilm research from various perspectives. Molecular genetics approaches to biofilm research yielded genetic pathways that are involved in biofilm formation (*23*), studies of quorum sensing within biofilms provided insights into the molecules used by cells for communication (*24-27*), and biochemical studies yielded compositional and structural knowledge of ECM isolated components (*10, 11, 28-32*).

An emerging perspective of biofilm development considers them as multicellular organisms, because of their ability to differentiate into subgroups of cells expressing specific set of genes. In particular, differentiation in *B. subtilis* biofilms has been shown to give rise to distinct subpopulations that express different sets of genes related with specific functions, such as motility, matrix production, and sporulation (*20, 33*); Here also, heterogeneous matrix gene expression has been linked to heterogeneity in the mechanical robustness of subpopulations (*34, 35*). Current views of

differentiation of biofilms into subgroups therefore link between genetic division of labor and phenotypic heterogeneity at the single cell as well as the subpopulation level, however, it neglects a molecular view of structural heterogeneity across entire biofilms.

We hypothesized that the division of labor across biofilms may lead to molecular ordering within specific domains in the biofilm. To test this hypothesis, we studied the local molecular structure and elemental composition across biofilms in a spatially resolved manner. We used micro-focus x-ray diffraction (XRD) and x-ray fluorescence (XRF) to scan along intact biofilm samples of different ages, using *B. subtilis* as a model organism for biofilm formation. We revealed that the internal spatio-temporal division of labor in *B. subtilis* biofilms is manifested by structural variations across biofilms and between biofilms of different ages, that depend mainly on the presence of spores and ECM components. Spores harbored highly ordered structures, while ECM conveyed minimal cross-β sheet structure, that only partially depended on the presence of the major proteinaceous ECM component, TasA. XRF measurements exposed preference of biofilms in general and biofilm sub-populations in particular to specific metal ions, calcium, magnesium, manganese, iron and zinc. Our study provides a molecular view of multicellularity in biofilms, demonstrating a link between biofilm morphology, molecular structure and metal ions preference that depend on the division of labor of subgroups across whole biofilms *in situ*.

Results and Discussion

Hydration sensitive spore-coat XRD contribution dominates the diffraction pattern of mature *Bacillus subtilis* biofilms.

We scanned a 2.5x6 mm^2 area in an intact sealed and hydrated biofilm using a micro-focused beam while simultaneously acquiring XRD and XRF, as described in the schematic presented in Fig. 1. We chose a mature WT biofilm sample (10 days old) where the dominant morphological features, mm-scale, large and small wrinkles were preserved (marked L, S, respectively in Fig. 1). For each

measurement point along the scanned region (X-ray beam cross-section = 50x50 μm^2, step size = 200 μm, 300 μm on X, Y axis, respectively), we simultaneously obtained a two-dimensional (2D) diffraction pattern collected on an area detector and an XRF spectrum. The 2D patterns were mostly completely isotropic, indicating that within the biofilm plane there was no preferred alignment of structural components. We therefore azimuthally integrated the 2D patterns (in the full range 0-360°) to obtain a one-dimensional (1D) profile of the intensity (*I*) versus scattering vector (*q*). Peaks on the 1D profile correspond to reflections from ordered structures in the biofilm, with characteristic d-spacings (units of length) in real space inversely related to *q* ($d = 2\pi/q$).

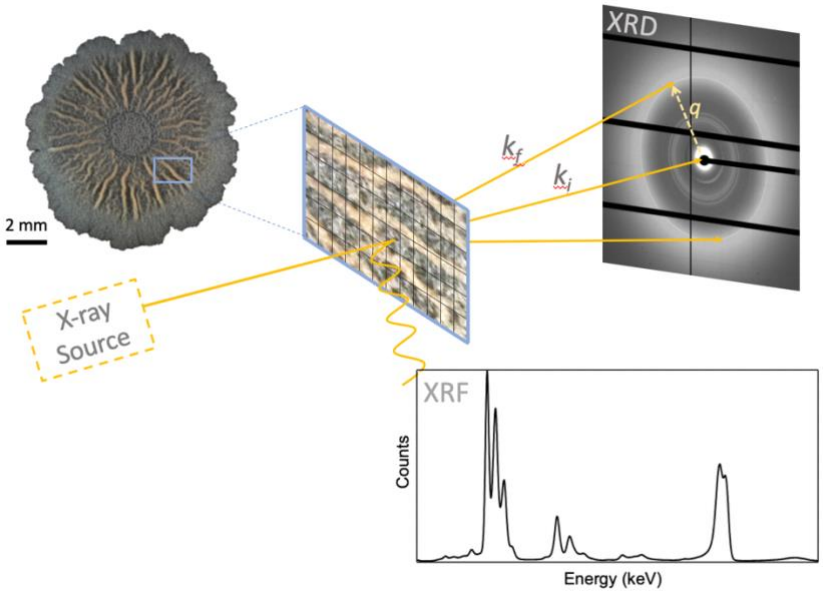

Figure 1. Schematic representation of the experimental set-up. A slice from an intact biofilm sample is placed between an X-ray source and a two-dimensional area detector in transmission geometry. XRD signal is collected simultaneously with X-ray fluorescence (XRF) using a fluorescence detector located perpendicular to the incoming beam. The X-ray beam is scanned along the sample yielding structural and compositional information with spatial resolution determined by the size of the beam cross section and scanning the step size. k_i and k_f are the direct beam and scattering vectors, respectively. *q* is the defined as the difference between k_f and k_i.

The diffraction patterns of the intact, hydrated, 10 days old wild-type (WT) biofilm sample showed scattering signals in both low (q = 4 - 8 nm^{-1}, marked with a rectangle) and high (q = 10 - 30 nm^{-1}) q-ranges (Figs. 2A-2C). In the low q range, WT biofilms exhibited several reflections, residing around ~ 6 nm^{-1}, corresponding to structural order with *d*-spacing in the order of 10 Å in real-space, which typically contained a sharp doublet superimposed on a broader hump.

The XRD pattern of dry WT biofilms largely corresponded with the XRD profile reported before for isolated spore samples (*36*), and confirmed by us (Figs. 2c, 2d and S3). The relative intensities of the two peaks comprising the doublet were similar across the biofilm sample (Fig. S2(C)), implying that they originate from a single spore-component or from components with similar relative abundance. Notably, the peak at ~ 7.5 nm^{-1}, may be explained by periodicities of the order of ~ 8 Å, that have been observed by rodlet and honeycomb protein assemblies in *B. subtilis* spore coat (*16*).

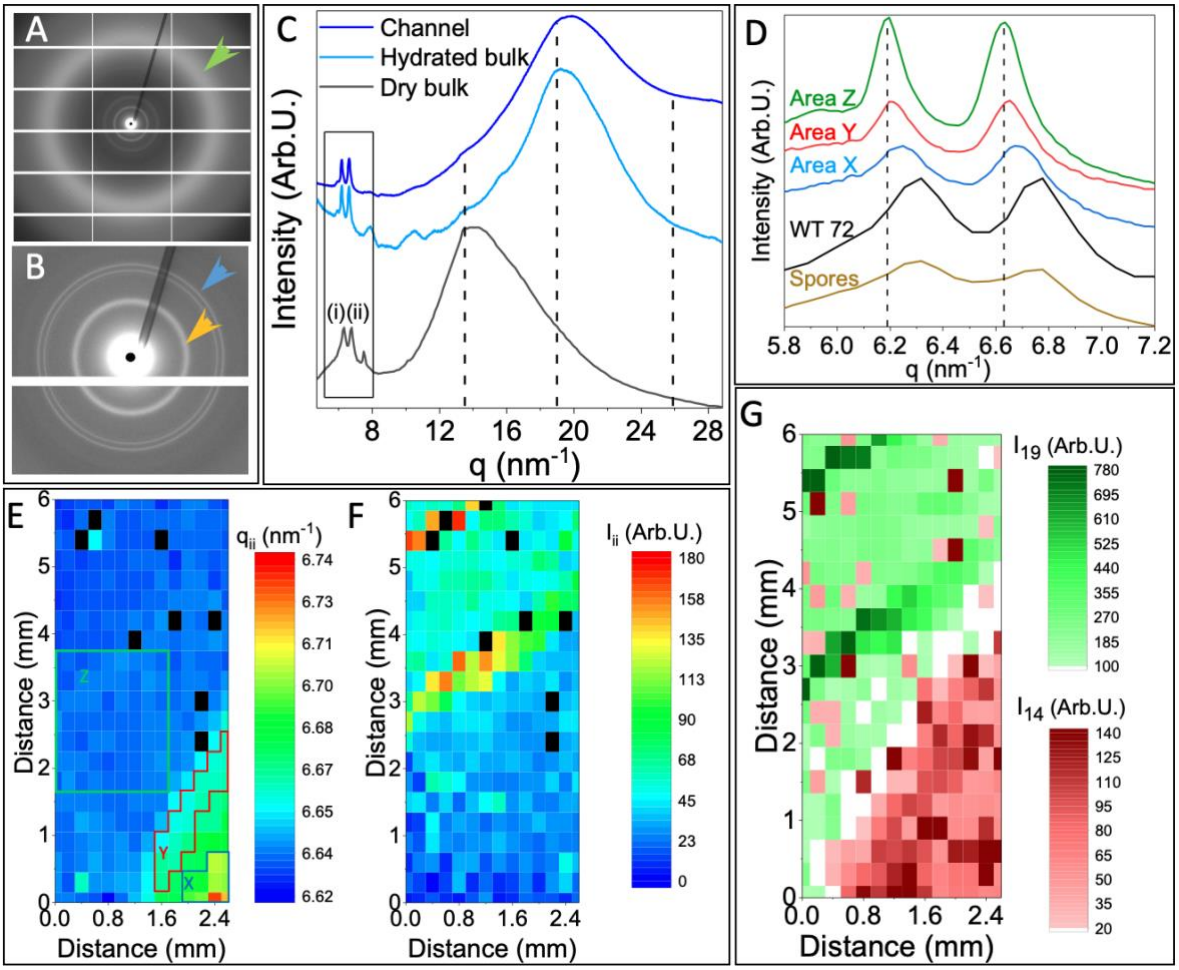

Figure 2. **XRD of intact hydrated WT biofilm.** (A, B) 2D pattern of a natively hydrated biofilm, green arrowhead shows the water signal (A) full detector image (B) zoom-in into the low q range, showing the dominant doublet (marked with a blue arrowhead); Orange arrowhead marks the sample carrier (Kapton film) signal. White grid lines are borders between detector units. (C) Representative azimuthally integrated 1D diffraction profiles, of a native hydrated (top, dark and light blue curves) and fixed, dehydrated (bottom, black curve) biofilms. The profiles show a doublet peak in the low q range (marked with a blue arrow in (A)) and broad signals in the high *q* range (marked with green arrowhead in (A)). Dashed lines point at peak positions q = 13.5 nm^{-1}, and q = 19 nm^{-1}, corresponding to d-spacing of ~ 4.7 Å and 3.3 Å, respectively. The former is attributed to biofilm biopolymers and the latter is attributed to water signal. (D) Zoom into the low q range (marked with a rectangle in (C)), showing the average profiles in different areas in the biofilm sample (X, Y, Z, corresponding to the blue, red, green curves, respectively), the average peak positions in a fixed and dry biofilm (black curve) and in a spore sample (olive green curve). (E) Mapping of the low q peak at ~ 6.7 nm^{-1} (peak (ii), marked in (C)), corresponding

to ~ 9.4 Å d spacing, across a WT biofilm slice of 2.6 X 6 mm^2 area (F) Intensity maps of peak (ii) (around q = 6.7 nm^{-1}) showing higher intensity along biofilm's wrinkles. (G) Mapping of the dominant peaks in the high q range, q = 14 nm^{-1} and q = 19 nm^{-1} highlight the drying versus hydrated areas where the 14 nm^{-1}, 19 nm^{-1} positions are dominant, respectively; Water signal at 19 nm^{-1} is highest along the biofilm wrinkles, which serve as water channels (*37*).

We used peak-fitting to evaluate the variation in specific reflections across the sample, yielding peak position, width and amplitude for the dominant scattering signals for each of the measured pixels (position in the biofilm) (Fig. S1). Mapping the spatial variation of the dominant doublet reflections in the biofilm showed that the doublet appeared across the whole biofilm sample, with the q values ranging between 6.19 to 6.24 nm^{-1} (peak (i), Fig. S2A-S2B) and 6.70-6.63 nm^{-1} (peak (ii), Figs. 2C, 2E). The doublet peak positions were rather uniform across the measured area, yet they exhibited a small gradient, shifting to higher q values along the direction going from the top left corner of the biofilm sampling area to the bottom right (Figs. 2D and 2E). The intensity of the doublet showed an increase along large wrinkles in the biofilms relative to areas away from or between the wrinkles (Fig. 2F).

In the high q range, the diffraction profiles of the hydrated sample showed typically broad peaks that we deconvoluted using peak-fitting (Fig. S5). In all the biofilms we tested, namely, fixed and dry (curve 'dry bulk' in Fig. 1C), as well as natively hydrated biofilms ('hydrated bulk' and 'channel' in Fig. 1C), the broad peak included contributions around 14 nm^{-1}, corresponding to reflections from biopolymers present in the ECM and to ordered structures inside the cells. The sugar-phosphate backbone in DNA, for example, which is present both inside and outside the cells (*38*), bears a characteristic reflection at 15 nm^{-1} (*39*), and polysaccharides purified from biofilms showed typical scattering at q ~ 13 nm^{-1} (Fig. S6). In addition to the contribution at q ~ 14 nm^{-1}, natively hydrated biofilms had additional contributions around q = 19 nm^{-1} and q = 26 nm^{-1}, corresponding to scattering form water (*40, 41*). Previous reports have shown that hydration layers in proteins give rise to scattering signal around q = 19 nm^{-1} (*40*), while free, liquid water gives rise to reflections at q = 19 nm^{-1} as well as q = 26 nm^{-1}, originating from the hydrogen bonding of water with typical distance of between oxygen atoms around 2.8 Å (*41*). Strikingly, the relative contribution of these reflections depended on the position

in the biofilm. In biofilm pixels located directly above the wrinkles (curve 'channel' in Fig. 1C), free water (q = 19 nm-1 and 26 nm^{-1}) contributed the most to the high q range. In fact, fitting results show that the relative amplitude of these two peaks is comparable to that of pure liquid water. In bulk areas away from the channels (curve 'hydrated bulk'), the free water signal at 26 nm^{-1} was not apparent, leading us to conclude that the contribution at q ~ 19 nm^{-1} results from water bound to ECM biopolymers. This finding stands in agreement with a previous study, that showed that biofilm wrinkles serve as channels filled with water, essentially function to transfer nutrients across biofilms (*37*). In biofilms that age older than 6 days, these channels become closed tubes, which can explain the entrapment of free water that we observe with XRD (*37*).

Interestingly, the large variation in the intensity of the water signal (Fig. 2G), which corresponded with the total measurement time, suggests partial dehydration of the sample during the measurement. This dehydration provided an interesting insight into the hydration/dehydration process in biofilms. Mapping the intensity of the peak contributions in the high q range across the sample (Fig. 2G) revealed that the 14 nm^{-1} reflection was dominant in the top left part of the sample and that of the 19 nm^{-1} at the bottom right part of the sample. In the hydrated regions (with high water scattering signal), the 14 nm^{-1} peak was still visible but partially obscured by the presence of the broad intense 19 nm^{-1} peak (water signal). The hydration gradient increasing along the diagonal of the biofilm sample coincides with shifting of the doublet peak position to lower q values (i.e., larger atomic separations) as the sample becomes more hydrated. In fixed samples of 72hr WT biofilms (Fig. 2C, 2E) and in isolated spore samples, these peaks show up at the highest q positions (6.3 nm^{-1} and 6,8 nm^{-1}). This observation is in agreement with the suggestion that the doublet signal is attributed to highly organized spore coat proteins (*16, 36, 42, 43*) and therefore can be expected to be sensitive to biofilm hydration. An intriguing hypothesis then arises that spore coat proteins may serve as humidity sensors based on their swelling.

Metal ions preferentially accumulate in biofilm wrinkles

We measured the XRF signal from biofilms concurrently with XRD in order to probe the distribution of accumulated metal ions across biofilms (Fig. 3). The fluorescence counts were then converted to relative atomic density taking into account the energy dependent absorption cross-section for each element (*44-47*). We found a higher signal of the metals zinc, iron and manganese along the biofilm wrinkles. A similar trend is observed for magnesium (Fig. S2 (D)), however due to the low fluorescence emission energy of Mg leading to significant absorption in air, the magnesium results are less reliable. For comparison, calcium and potassium are also present in the biofilms to a large amount (Figs. 3, Fig. S2 (E), respectively) but their distribution does not correlate with the wrinkle morphology, suggesting that the localization of Zn, Mn, and Fe in the wrinkles is preferential over other metal ions. Interestingly, we find that while Ca is the most abundant metal ion in the films, it is not preferably found along large wrinkles, i.e. water channels, where spores show the strongest XRD signal.

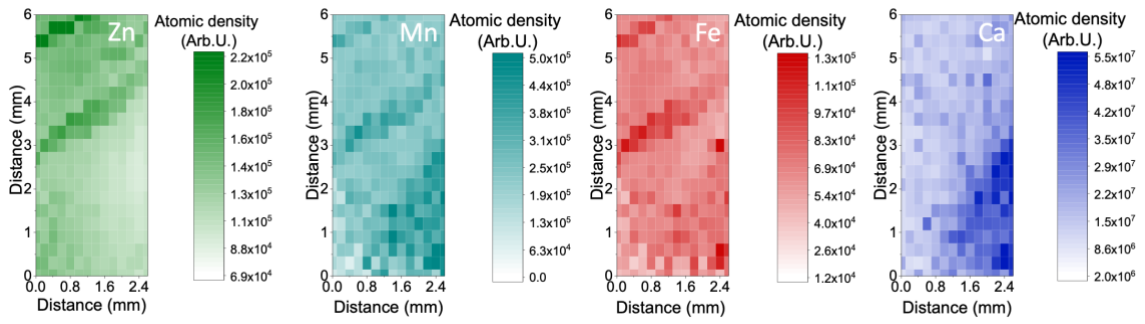

Figure 3. Atomic density measured by XRF of intact hydrated WT biofilm slice. Elemental distribution maps of the corrected fluorescence signals of Zn (green), Mn (Cyan), Fe (red), Ca (blue) of WT biofilms. The signal of Zn, Mn, and Fe, but not Ca, is stronger in the biofilm wrinkles, coinciding with water and spore accumulation along biofilm wrinkles.

The elevated signal of some metal ions along the wrinkles, measured by XRF, coincided with increased intensity of the doublet XRD signature acquired simultaneously. It is unlikely that this observation can be attributed to larger biofilm thickness along wrinkles, since this should also lead to concomitant increase in Ca signal. Thus, our results could suggest that accumulation of Zn, Mn, both of which have been described to play a role in sporulation (*48-50*) (Fig. S7), as well as Fe may indeed be related to the presence of spores. This result is also intriguing in the light of recent finding showing that calcium

ions inhibit spore dispersal (*50*). It is interesting to speculate whether the continued evaporation of water along the wrinkles, serving as lateral water channels, lead to salt accumulation that in turn triggers sporulation. At the same time, spores may serve to store metal ions, thereby regulating salt concentrations that may otherwise become toxic.

Loss of spore-associated reflections exposes weak cross β sheet structure in matrix mutants and in young biofilms

Assigning the XRD doublet to spores, we studied matrix mutant biofilms, Δeps and ΔtasA, reported to negligibly express sporulation genes (*20*). Transmission electron microscopy (TEM) imaging of WT biofilms, taken at various positions (Figs, 4A_i, large wrinkles, denoted by 'L', and Fig. S9. Small wrinkles, denoted by 'S') and mutant biofilm samples (Figs. 4B_i, 4C_i), reveal several cell types, in particular, normal cells (examples marked with orange arrows), empty cells (examples marked with blue arrows), deformed cells (examples marked with yellow arrows), sporulating cells (examples marked with green arrows) and spores (examples marked with purple arrows). Figs. A_i-C_{iv}, as well as a quantitative analysis of the cell types in different TEM images (total number of cells was 4715 in a total of 189 images) (Fig. S4) show clearly that the abundance of sporulating cells and spores in biofilms made by the ECM mutants, Δeps and ΔtasA, is negligible relative to their abundance in WT biofilms.

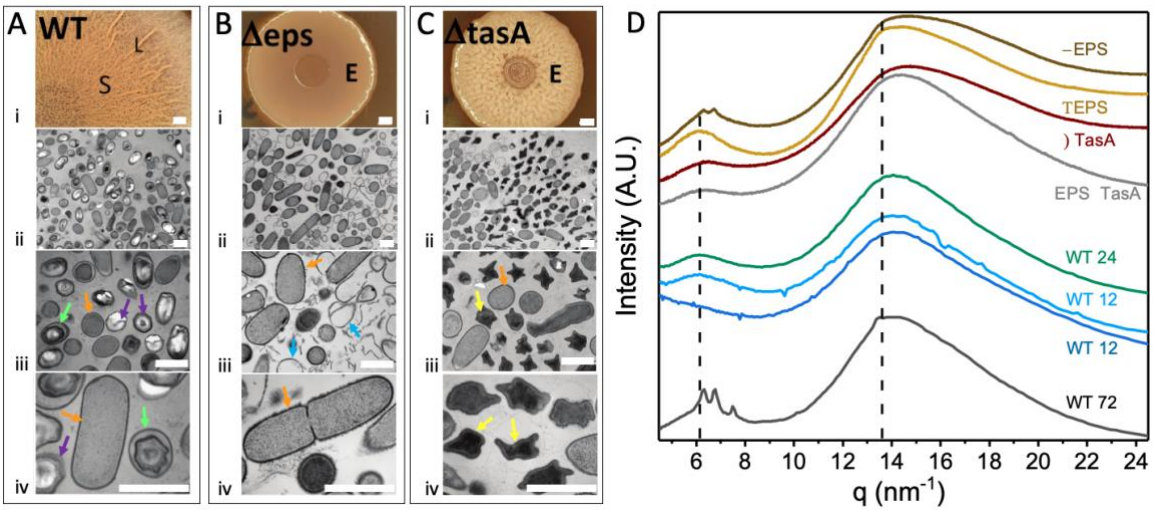

Figure 4. Matrix and cell contributions in biofilms. (A_i, B_i, C_i) Light microscopy of biofilm samples and (A_{ii}-A_{iv}, B_{ii}-B_{iv}, C_{ii}-C_{iv}) TEM imaging of fixed and stained thin sectioned WT (a2-a4), Δeps (b2-b4) and ΔtasA (c2-c4) mutant biofilms, taken in different locations, as indicated on the light microscopy biofilm images. L, S, in a_i denote large and small wrinkles, respectively, E in B_i and C_i) denotes the edge of mutant biofilms that were examined in this study. We identified several cell types in the TEM images: normal cells (marked orange), empty cells (marked blue), deformed cells (marked yellow), sporulating cells (for example cells marked green) and spores (marked purple). Scale bar in all panels is 1μm (D) comparison of the XRD of fixed mature (72 hours old) WT biofilms, fixed mature biofilms made by matrix mutant cells, Δeps and ΔtasA, double mutant, ΔepsΔtasA, as well as by fixed young biofilms (aging 12 hours and 24 hours), where spores have not yet developed. Dashed line marks the position of the inter-sheet and intra strand peaks in cross β sheet structures (q ~ 6 nm^{-1} and 14 nm^{-1}).

The azimuthally integrated 1D XRD curves (Fig. 4D) showed loss of the spore-associated doublet in ΔtasA mutant biofilms (green curve in Fig. 4D). We observed two phenotypes for the Δeps mutant biofilms. In one phenotype, the double peak disappeared altogether (brown curve in Fig. 4D) while in the second, it was apparent as low intensity peaks superimposed on top of a broad hump (orange curve in Fig. 4D). The loss of the spore-associated doublet XRD peak is therefore related with the loss of spores in biofilms of the matrix mutants. Profiles lacking the dominant spore associated reflections, exposed XRD patterns that originated from other components in the biofilm, namely cells and matrix components. Interestingly, we identify the two broad reflections appearing at q ~ 6 nm^{-1} and ~ 14 nm^{-1}, that typically correspond to the canonic cross beta structure attributed to a 10 Å (intersheet) and 4.7 Å (interstrand) spacings, respectively. Biofilms of double mutant strains, that lacked both eps and tasA genes, still had the 6 nm^{-1} and 14 nm^{-1} reflections (grey curve in Fig. 4D). While all the mutant biofilms measured contained the low and high peak contributions, the relative intensity of the low peak contribution (namely around 6 nm^{-1}), was lower in mutants that lacked TasA (Figure 4D).

The mutant biofilms described above were poor in spores but they additionally lacked either the protein matrix component, TasA, the polysaccharide matrix component, EPS, or both. We hypothesized that TasA, the most abundant structural protein in *B.subtilis* matrix (*28*) is the major contributor to the cross-beta sheet signal in the biofilm. Indeed, the crystal structure of TasA contain a cross-beta sheet core, and it is suggested to form amyloid fibers *in vitro* (*28, 30*). In order to test this hypothesis we performed a temporal analysis of the biofilm at early time points, where according to Vlamakis et al., at 12 and 24 h, WT biofilms express TasA to a variable degree, but they do not yet

produce spores (*20*). XRD profiles indeed showed that the spore-associated doublet, was not yet present in young biofilms. At 24 hours, broad peaks appeared (blue curve, Fig. 4D), attesting the contribution of matrix and cells to the XRD signal. At 12 hours, the broad hump around 6 nm^{-1} was occasionally present, but in other regions the low q range did not contain any signal. Indeed, at 12 hours TasA expression is initiated but the matrix is not yet uniform across the whole biofilm area (cyan curves, Fig. 4E) (*20*). Probing the samples at this time point allowed to isolate the XRD signature of cells with little contribution of the matrix. The loss of the low *q* hump, indicated that higher order intramolecular structures, are dependent on the presence of matrix components and that the cells themselves do not contribute to the signal at low q that we then associate with inter-sheet signature in cross beta structure.

XRD data of WT biofilms of different age and matrix mutant biofilms were fitted with five peak positions covering the low and high *q* ranges (see experimental table S1, and Fig. S1) in order to compare the dominant peak positions. For simplicity, we only specify here the low *q* peak position without the doublet, and two peak positions in the high *q* range (this is a broad hump and a shoulder and therefore two positions were necessary to represent it). Both the low and high *q* peak positions, attributed to cross beta structures, were similar in fixed mature WT, matrix mutants (Δeps, ΔtasA and ΔepsΔtasA), and, when present, in young biofilms (see dashed lines in Fig. 4d located in the peak positions of 72 hours old WT biofilms). While, the cross-beta signature was more dominant in biofilms containing TasA, similar cross beta sheet signature is found also in biofilms made by tasA mutants (Fig. 4). We thus conclude that intact biofilms harbor a cross beta sheet structure, resulting from matrix components not limited to TasA.

TasA harbors a minimal cross-beta domain and binds metal ions

Facing the presence of cross beta sheet fingerprint in intact biofilms, its increase in the presence of TasA (in 24- and 72-hour WT samples) and in light of the literature debate on the amyloid nature of TasA (*28, 31, 51, 52*), we were intrigued to learn more about the structure and composition of fibers

formed *in vitro* from isolated TasA preparations. Recently, we have shown that TasA is polymorphic, as it forms fibers with different morphologies: aggregates in acidic solutions (termed 'aggregates' henceforth), thin and long fibers at high salt concentrations (termed 'fibrils' henceforth) and fiber bundles at high protein and salt concentration (henceforth termed' bundles') (*30, 53, 54*).

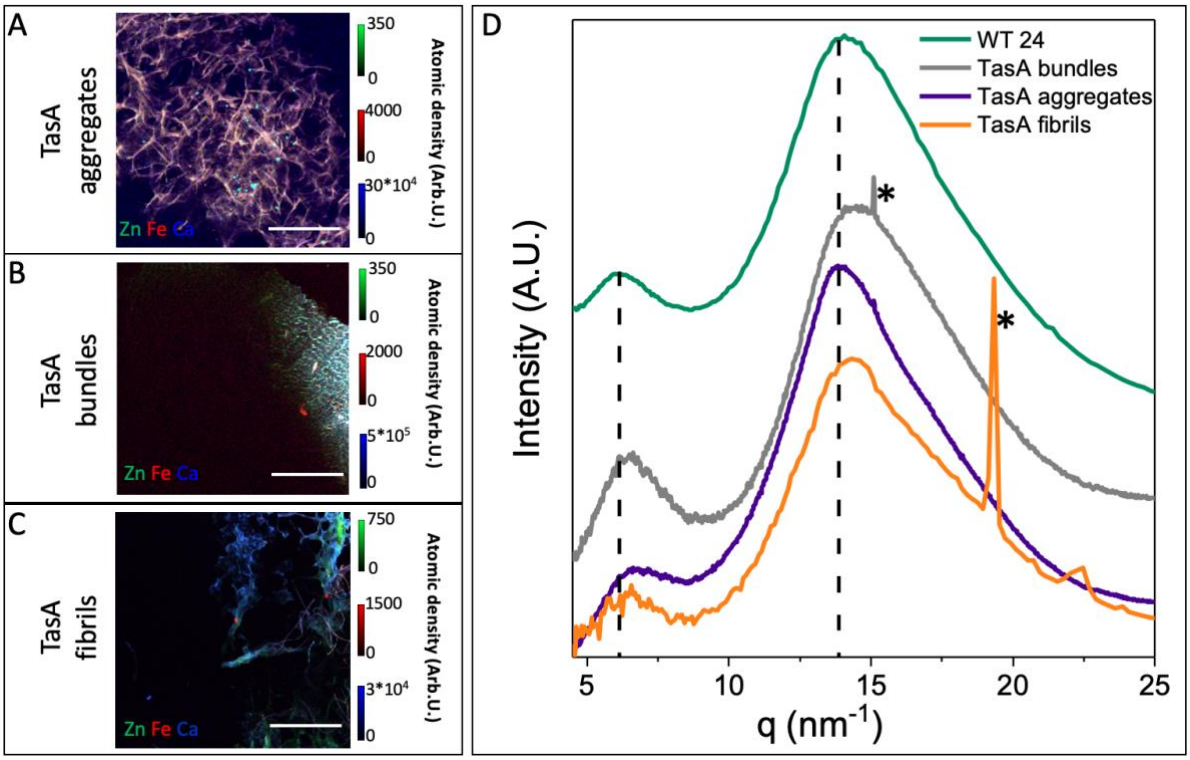

Figure 5. Morphology, metal ion binding and XRD profiles of TasA fibers formed in different environments. (A-C) XRF of TasA fibers, (A) formed in acidic conditions ('TasA aggregates), (B) high salt concentration ('TasA fibrils'), and (C) high protein and salt concentration ('TasA bundles'). Color code: zinc (green), iron (red) and Calcium (blue); red and blue = purple, red and green = yellow. (D) XRD profiles of TasA aggregates (purple curve), fibrils (orange curve), and bundles (gray curve) along with the XRD profiles of 24 hours old WT biofilms (green curve). The sharp peaks in the fibrils' profile, marked with * formed at high NaCl concentration are attributed to salt crystal impurities.

To examine a possible relation between binding of metal ions by TasA and by biofilms, we examined protein fibers preparations with XRF. Figure 5a-c shows an overlay of the dominant XRF signals of the metal ions that we observed accumulated in biofilms, Zn, Fe and Mn or Ca (see Fig. S8 for more detail). It became evident that TasA fibrils, bearing different morphologies (prepared in different environments, but also within the same preparation, e.g., Fig. 5C), contained the metal ions Zn, Fe

and Mn or Ca, that were also probed in WT and mutant biofilms (as shown in this and in other studies (*9*)). However, different TasA polymorphs had a different preference to these metal ions as shown in an overlay of the XRF maps of these metal ions (Figs. 5A-5C, Fig. S8). Calcium binding was dominant in all protein preparations. in addition, in aggregates that formed in an acidic environment, iron binding dominated over manganese and zinc (Fig. 5A), whereas bundles that formed in high salt (NaCl) and protein concentrations accumulated more iron and manganese ions relative to zinc (Fig. 5B, S8). Moreover, the fibrils that formed at high salt concentration were especially heterogeneous, as was reflected both in their morphology and metal ion binding (Fig. 5C). Specifically, in these fibers, iron (red) binding was observed within long fibers with high persistence length, while iron, zinc and calcium appeared to be distributed inhomogeneously in larger areas where the fibers assemble into a mesh (red and blue appear as purple). These results suggest that at least part of the metal ions in biofilms, and especially calcium ions are bound by TasA within the matrix. The variations in the XRF signal of TasA fibers, prepared in three different environmental conditions, is a further testimony of the protein's polymorphism.

Figure 5D shows the averaged 1D azimuthally integrated XRD signatures of isolated TasA that formed fibers *in vitro* under these three conditions. Despite large variations in fibril morphologies, the three preparations of TasA fibers exhibited two broad reflections close to q ~ 6 nm^{-1} and ~ 14 nm^{-1}, corresponding to the canonic cross beta sheet structure. Peak-fitting shows that these peaks were slightly shifted to higher *q*, relative to those of 24 h old WT biofilms (marked by vertical dashed lines, see also table S1), indicating a more compact packing of TasA fibers formed *in vitro* relative to biopolymers within the biofilm.

Diehl et al., reported that the XRD of TasA fibers formed from recombinant protein in acidic conditions has narrow intra- and inter-sheet reflections of a cross beta sheet configuration (*51*), which, in our case, are very broad. While the combination of these reflections is indicative of cross β sheet features, it is unlikely that they organize into long range ordered amyloid structure. This is consistent with our

previous suggestions that TasA fibers form in a oligomer-to-oligomer addition (*54*), but our data is insufficient to suggest a model for the interactions between monomers/oligomers. We attribute the disparity in the molecular organization of TasA fibers between that reported here and that demonstrated for amyloid fibers to the fact that our fibrils are composed of full length proteins, rather than short peptides (*55-58*) or truncated (recombinant) sequences (*51*). Considering the NMR studies and crystal structure of TasA as being composed of beta strands arranged in a jelly roll core, as well as alpha helices and loops (*51*), the cross-beta structure may arise from the internal core or from packing of intermolecular beta strands or sheets. Importantly, the similarity between the XRD patterns of TasA fibers formed *in vitro* and the matrix XRD signal obtained *in situ* suggests that also in intact biofilms, TasA and other structural components form ordered fibers that are nevertheless not amyloidic.

Conclusions

It has been previously demonstrated that cellular subpopulations form in time and space during biofilm development, giving rise to spatio-temporal division of labor. Specific subpopulations include matrix and spore-forming cells, the latter appearing mostly in aerial hyphae at the surface of biofilms. Here we show that spatial differentiation by function also imposes structural and elemental heterogeneity in intact biofilms. When probed by X-ray diffraction, *B. subtilis* biofilms show a characteristic structural signature originating primarily from ordered structures within the coat of spores, that are sensitive to the hydration level of the film. The spores are present throughout the biofilm but concentrate along large wrinkles that serve as water channels. The spores signal is lost in biofilms lacking the matrix components as in ΔtasA and Δeps, as well as in young biofilms, where sporulation has not yet been initiated (as also shown by TEM). We speculate that the wrinkly morphology of elevated areas serving as water channels, which are absent in these mutant and young films, are essential for ion transport and spore formation. The loss of the spore-associated signal allows distinguishing between the contribution of the bacterial cells and reveals an additional cross β sheet structure that is attributed to the biofilm extracellular matrix. Our study establishes a link between the presence of the TasA and the cross β sheet structure in intact biofilms, however, it is unlikely that full-length TasA fibers possess long range amyloidic order either *in vitro* or *in situ*. Furthermore, while TasA is the major component contributing TasA to the cross β structure in the biofilm, there are other additional ECM components which may also exhibit a cross β sheet structure. We have shown that even though biofilms are soft matter communities, they show molecularly-

structured matrix regions that are linked to metal ion distribution as well as to the spatio-temporal division of labor in biofilms. This study may open the way for better understanding of biofilm physiology at the molecular level.

Materials and methods

Bacterial *Bacillus subtilis* strains used in this study

Wild-type (NCIB361O)

eps mutant SSB488 (361O epsA-O::tet)

tasA mutant CA017 (361O tasA::kan)

sinReps double mutant (ZK4363)

Biofilm sample preparation

A 2 µl drop of bacterial cell suspension, grown as liquid culture overnight at 37 °C in Luria-Bertani (LB) medium, was spotted on solid MSgg medium agar (1.5%) plate (*19*), dried and kept at 30 °C or room temperature between 12 h – 10 days, as indicated in the text.

Spores sample preparation.

Wild-type *Bacillus subtilis* LB liquid culture, grown for 8 h at 37 °C, was spread (200 µl suspension) on solid LB agar (1.5%) plate and kept for 48 h at 37 °C.

TasA Purification and sample preparation.

TasA was purified as described previously (*28, 30*). Briefly, sinR eps double mutant *B.subtilis* cells (ZK4363) were grown in MSgg broth, at a 1:100 dilution from an LB overnight culture, under shaking conditions. After 16 h of growth at 37 °C the cells were pelleted (10000g, 15 min, 4 °C), resuspended with saline extraction buffer and probe sonicated (1518J, 5 s pulse and 2 s pulse off). Following an

additional centrifugation step (10000g, 15 min, 4 °C), the supernatant was then collected and filtered through a 0.45 µm polyethersulfone (PES) bottle-top filter. The filtered supernatant was collected after centrifugation (17,000 g, 15 min, 4 ◦C), concentrated with Amicon centrifugal filter tubes and either incubated in saline extraction buffer for 72 h at 4 °C (used to prepare 'TasA bundles') or passed through a HiLoad 26/60 Superdex S200 sizing column that was pre-equilibrated with a 50 mM NaCl, 5 mM HEPES solution at pH 8 (used to prepare 'TasA aggregates' and 'TasA fibrils'). Purified proteins were stored at −20 °C until use. The concentration of the protein was determined using a BCA protein assay (ThermoFisher Scientific, Waltham, MA, USA).

Polysaccharide purification

Polysaccharide was purified from WT Bacillus Subtilis pellicles, as previously described (*12, 32*). WT liquid culture was grown overnight in LB medium and transferred to SYN medium at a 1:100 dilution. Pellicles were collected after 24 h at 37 ˚C, transferred into fresh SYN medium and washed twice by centrifugation at 5000 rpm for 15 min at 25 ˚C. The pellet was collected probe sonicated (1518J, 5 sec pulse and 2 sec pulse off) (Sonics, Vibra cell CV334) in fresh medium for 150 sec. The supernatant was separated from the pellet after an additional sonication and centrifugation of 5000 rpm for 30 min at 25 ˚C. The EPS was precipitated by adding x3 ice-cold isopropanol (J.T. Baker) following an overnight at -20 ˚C. The supernatant was discarded and the precipitate was washed twice with ice-cold isopropanol and was kept at -20 ˚C for additional 2 h. The precipitant was collected, dissolved in 0.1 M MgCl2 (J.T. Baker) and extracted twice by phenol-chloroform (Fisher Chemical) on a separating funnel. The aqueous phase was collected, dialyzed for 48 h against DDW (with a Cellu Sep T3, 12000-14000 MWCO.) and lyophilized to dryness. For purification from DNA and proteins, EPS was dissolved in a 10 mM Tris buffer (VWR) containing 50 mM NaCl, 10 mM MgCl2 pH 7.5 and incubated with DNase (Sigma-Aldrich) at 37 ˚C for 1 h. Proteinase K (Sigma-Aldrich) was then added and the solution was incubated at 40 ˚C for 1 h. The solution is dialyzed against DDW (with a Cellu Sep T3, 12000-14000 MWCO.) for 48 h and lyophilized to dryness.

TasA fibers preparation

TasA fibers were prepared as previously described(*54*), under the following conditions:

TasA bundles: Purified TasA was incubated in saline extraction buffer for 72 h at 4 °C. The solution was then dialyzed against TDW for three days, lyophilized and placed between two silicon nitride membrane or resuspended in a drop of water and mounted on a loop (Hampton Research).

TasA fibrils: Purified TasA was passed through a HiLoad 26/60 Superdex S200 sizing column that was pre-equilibrated with a 50 mM NaCl and 5 mM HEPES solution at pH 8. Sodium chloride stock solution (5M) was then added to the protein yielding the final concentration, 1.5 M NaCl and 130 µg/ml TasA. The solution was incubated for 72 h at 4 °C and dialyzed against TDW for three days, lyophilized and placed between two a silicon nitride membrane.

TasA aggregates: Purified TasA was passed through a HiLoad 26/60 Superdex S200 sizing column that was pre-equilibrated with a 50 mM NaCl and 5 mM HEPES solution at pH 8. The solution pH was then adjusted to 2.5 with formic acid, yielding TasA aggregates (*53*) and kept at room temperature for three days at 4°C. The solution was exchanged by consecutive centrifugation (5000 rpm, 10 minutes) and supernatant replacement with TDW, three times every 24 hours. The solution was then lyophilized and placed between two silicon nitride membranes or resuspended in a drop of water and mounted on a loop (Hampton Research).

SAXS/XRD and XRF mapping

Scanning XRD/XRF measurements of biofilms and proteins were performed at the mySpot beamline synchrotron BESSY II (Helmholtz Center, Berlin, Germany) and at the ID13 beamline Synchrotron ESRF (Grenoble, France).

At ID13 the X-ray beam (ESRF) was defined to 13.0 keV (0.954 Å) using a monochromator and focused to 2x2 μm^2 or 5x5 μm^2. 2D patterns were acquired in transmission mode using a 4M Dectris, Eiger detector (pixel dimension), by integrating for 2 sec in an “on-the-fly” scanning mode. A Vortex EM,

silicon drift detector with 50 mm^2 sensitive area, XRF detector was placed roughly 90 degrees to the incoming X-ray beam to collect the emitted X-ray photons from the sample simultaneously. Acquisition time was set to 2 sec/point.

At mySpot beamline the X-ray beam (Bessy II) was defined to 15.0 keV (0.827Å) using a B4C/Mo Multilayer monochromator and focused to 50x50 μm^2 using KB mirrors and 50 μm^2 pinhole. XRD data were obtained using a 2D Dectris Eiger 9 M detector ((2070 × 2167) pixel2) in transmission geometry, and a single element Si(Li) XRF detector (RAYSPEC (SGX Sensortech) was placed perpendicular to the beam. Acquisition time was set to 60 sec/point.

Sample to detector distance (around 300mm) was calibrated using quartz powder in both setups. When present, internal kapton signal at q = 4 $nm^{-1}$was used to further verify the calibration for each sample. Calibration of XRF detectors was performed using pyMCA (http://pymca.sourceforge.net/) using the argon emission and the main beam scattering energy. XRF intensities were corrected by the theoretical absorption cross-section for each element, at 15 or 13 KeV (*44-47*) taking into account (when relevant) the absorption of the XRF by the detector Berillium window (8 μm thick).

Sample preparation for XRD measurements

Biofilm samples were mounted on aluminium frames overlaid with kapton films (13 μm thick from Goodfellow Cambridge limited or 25 μm thick from DuPont) or on a silicon nitride membrane (Silson Ltd., frame: 10.0 mm x 10.0 mm, 200 μm thick; membrane: 5.0 mm x 5.0 mm, 1000 nm thick). Hydrated biofilm, measured at myspot, was sealed at the lab an hour prior to the measurement between two kapton films. The biofilm was gently pulled off the agar plate and placed on silicon nitride membrane of kapton film. During biofilm removal, only WT biofilms maintained their shape and humidity level. Fixed samples were prepared by overnight exposure to 15% formaldehyde vapour following mounting on kapton foil/Silicon nitride membrane.

Spore sample was scrapped from the plate and placed between Kapton sheets that were glued on an aluminium frame and sealed with a parafilm. Protein samples measured at ESRF were prepared in glass capillaries (Hilgenberg GmbH, 0.01 mm wall thickness) or sandwiched between two 1000 nm thick silicon nitride membranes (see above).

SAXS/WAXS/XRF analysis.

Calibration, integration background removal, and peak-fitting of the 2D diffraction patterns were performed using the software DPDAK (*59*) or home-written routines based on pyFAI (https://pyfai.readthedocs.io/en/master/). The fitted parameters as well as the integrated XRF signal around specific emission lines, were exported and plotted in Origin 2020 to create the maps in Fig. S 1 and 2, the q and the intensity values of the peak-fitting of each point measured was used and plotted using origin 2020 software. For 1D presentation, the 1D patterns from specific ROIs (X, Y, Z in Fig. 1E) were averaged and normalized by subtracting the minimum value and dividing by the maximum intensity. ROIs were chosen after removing dust and salt contamination based on XRF signals.

The protein XRF maps were converted to 3-channel image RGB (red, blue and green) images using the software ImageJ (*60*). The correction of the fluorescence intensity signal to relative atomic density was performed as described above. We note that absolute values cannot be directly compared between beamline set ups and sample as they depend amongst others on the incoming flux, the sample to detector distance and exact geometry, and the sample thickness.

Transmission Electron Microscopy of Biofilm colonies

Agar slabs (less than 0.5 mm^2) containing defined regions of the bacterial colonies were cut out and inverted on lecithin-coated 3-mm specimen carriers for high pressure freezing in a high-pressure freezing machine (Leica, ICE) with or without 10% polyvinylpyrrolidone as a filler (ΔEps biofilms and

one of the WT samples were frozen without filler). Samples were transferred under liquid nitrogen into a freeze substitution unit (Leica, AFSII) with 0.1% osmium tetroxide in acetone for substitution medium. Samples were slowly warmed from -90 °C to 0 °C within 3 days.

The samples were washed with acetone for one hour and incubated with 0.5% uranyl acetate in acetone for 1 hour still at 0 °C. Samples were washed 3x with acetone (moving from 0 °C to room temperature), before they were infiltrated with 25% and 50% epoxy resin (Roth, Germany) in acetone for 90 min. Samples were left in 75% epoxy resin overnight. Four changes of 100% epoxy resin followed over the period of 2 days before samples were flat-embedded between Teflon-coated microscope slides.

Infiltrated samples were polymerized at 60 °C for two days and defined regions mounted on resin stubs for cutting 70 nm–ultrathin cross-sections through the bacterial colonies, which were post-contrasted with 0.5 % uranyl acetate and 0.04% lead-citrate. Samples were investigated on a Morgagni transmission electron microscope (Thermofisher/FEI/Philips) at 80 kV and micrographs acquired with a Morada CCD camera (EmSis/Olympus) with ITEM software (EmSis/Olympus/Sys). Images were analysed using Fiji software (*60*)).

TEM images analysis according to cell type

Unbiased micrographs (image area 6 x 4.7 um with a 1.87nm/px resolution) of the biofilm samples were acquired using the xy-coordinate display at the TEM, with a step size of 20 μm. Cells were marked and counted in these TEM images (N, total number of cells = 7159). Cell types were classified as normal cells, empty cells, deformed cells, sporulating cells or spores, as indicated in the text and in Fig. 4. The number of cells of each type was normalized by the number of images evaluated, which normalizes the total area that was probed. Normalizing by the area takes into account differences in cellular density and therefore we chose to normalize by area and not by total cell number.

Acknowledgments

Measurements were carried out at the mySpot beamline at the BESSY II electron storage ring operated by the Helmholtz-Zentrum Berlin für Materialien und Energie and at beamline ID13 at the European Synchrotron Radiation Facility. We thank the HBZ and the ESRF for provision of synchrotron radiation facilities and for financial support. We thank EM facility of MPI-CBG for support, use of equipment and reagents, Daniel Werner at the MPIKG for X-ray measurements. Special thanks to Prof. Sigal Ben Yehuda for insightful discussions, Yosef Edri for help with data sorting and Daniel Rosenblatt for assistance with the image analysis.

References

1. T. Romeo, *Bacterial biofilms. Preface* (Curr Top Microbiol Immunol, Springer-Verlag Berlin Heidelberg, ed. 1, 2008), vol. 322.
2. J. W. Costerton, Z. Lewandowski, D. E. Caldwell, D. R. Korber, H. M. Lappin-Scott, MICROBIAL BIOFILMS. *Annual Review of Microbiology* **49**, 711-745 (1995).
3. S. S. Branda, Å. Vik, L. Friedman, R. Kolter, Biofilms: the matrix revisited. *Trends in microbiology* **13**, 20-26 (2005).
4. H.-C. Flemming, J. Wingender, U. Szewzyk, P. Steinberg, S. A. Rice, S. Kjelleberg, Biofilms: an emergent form of bacterial life. *Nature Reviews Microbiology* **14**, 563-575 (2016).
5. H. Boudarel, J.-D. Mathias, B. Blaysat, M. Grédiac, Towards standardized mechanical characterization of microbial biofilms: analysis and critical review. *npj Biofilms and Microbiomes* **4**, 17 (2018).
6. J. N. Wilking, T. E. Angelini, A. Seminara, M. P. Brenner, D. A. Weitz, Biofilms as complex fluids. *MRS Bulletin* **36**, 385-391 (2011).
7. A. Seminara, T. E. Angelini, J. N. Wilking, H. Vlamakis, S. Ebrahim, R. Kolter, D. A. Weitz, M. P. Brenner, Osmotic spreading of Bacillus subtilis biofilms driven by an extracellular matrix. *Proceedings of the National Academy of Sciences* **109**, 1116 (2012).
8. S. M. Rubinstein, I. Kolodkin-Gal, A. McLoon, L. Chai, R. Kolter, R. Losick, D. A. Weitz, Osmotic pressure can regulate matrix gene expression in Bacillus subtilis. *Mol Microbiol* **86**, 426-436 (2012).
9. N. Ido, A. Lybman, S. Hayet, D. N. Azulay, M. Ghrayeb, S. Liddawieh, L. Chai, Bacillus subtilis biofilms characterized as hydrogels. Insights on water uptake and water binding in biofilms. *Soft Matter* **16**, 6180-6190 (2020).
10. L. Hobley, A. Ostrowski, F. V. Rao, K. M. Bromley, M. Porter, A. R. Prescott, C. E. MacPhee, D. M. van Aalten, N. R. Stanley-Wall, BslA is a self-assembling bacterial hydrophobin that coats the Bacillus subtilis biofilm. *Proc Natl Acad Sci U S A* **110**, 13600-13605 (2013).
11. K. Kobayashi, M. Iwano, BslA(YuaB) forms a hydrophobic layer on the surface of Bacillus subtilis biofilms. *Mol Microbiol* **85**, 51-66 (2012).

12. D. N. Azulay, R. Abbasi, I. Ben Simhon Ktorza, S. Remennik, A. Reddy M, L. Chai, Biopolymers from a Bacterial Extracellular Matrix Affect the Morphology and Structure of Calcium Carbonate Crystals. *Crystal Growth & Design* **18**, 5582-5591 (2018).
13. Y. Oppenheimer-Shaanan, O. Sibony-Nevo, Z. Bloom-Ackermann, R. Suissa, N. Steinberg, E. Kartvelishvily, V. Brumfeld, I. Kolodkin-Gal, Spatio-temporal assembly of functional mineral scaffolds within microbial biofilms. *npj Biofilms and Microbiomes* **2**, 15031 (2016).
14. J. C. Nickel, I. Ruseska, J. B. Wright, J. W. Costerton, Tobramycin resistance of Pseudomonas aeruginosa cells growing as a biofilm on urinary catheter material. *Antimicrob Agents Chemother* **27**, 619-624 (1985).
15. P. T. McKenney, A. Driks, P. Eichenberger, The Bacillus subtilis endospore: assembly and functions of the multilayered coat. *Nature Reviews Microbiology* **11**, 33-44 (2013).
16. M. Plomp, A. M. Carroll, P. Setlow, A. J. Malkin, Architecture and Assembly of the Bacillus subtilis Spore Coat. *PLOS ONE* **9**, e108560 (2014).
17. A. G. Stöver, A. Driks, Secretion, localization, and antibacterial activity of TasA, a Bacillus subtilis spore-associated protein. *Journal of bacteriology* **181**, 1664-1672 (1999).
18. A. Driks, Bacillus subtilis spore coat. *Microbiology and molecular biology reviews : MMBR* **63**, 1-20 (1999).
19. S. S. Branda, J. E. Gonzalez-Pastor, S. Ben-Yehuda, R. Losick, R. Kolter, Fruiting body formation by Bacillus subtilis. *Proc Natl Acad Sci U S A* **98**, 11621-11626 (2001).
20. H. Vlamakis, C. Aguilar, R. Losick, R. Kolter, Control of cell fate by the formation of an architecturally complex bacterial community. *Genes Dev* **22**, 945-953 (2008).
21. G. O'Toole, H. B. Kaplan, R. Kolter, Biofilm Formation as Microbial Development. *Annual Review of Microbiology* **54**, 49-79 (2000).
22. J. A. Shapiro, THINKING ABOUT BACTERIAL POPULATIONS AS MULTICELLULAR ORGANISMS. *Annual Review of Microbiology* **52**, 81-104 (1998).
23. H. Vlamakis, Y. Chai, P. Beauregard, R. Losick, R. Kolter, Sticking together: building a biofilm the Bacillus subtilis way. *Nature Reviews Microbiology* **11**, 157-168 (2013).
24. S. Mukherjee, B. L. Bassler, Bacterial quorum sensing in complex and dynamically changing environments. *Nat Rev Microbiol* **17**, 371-382 (2019).
25. D. López, H. Vlamakis, R. Losick, R. Kolter, Paracrine signaling in a bacterium. *Genes & development* **23**, 1631-1638 (2009).
26. R. Bleich, J. D. Watrous, P. C. Dorrestein, A. A. Bowers, E. A. Shank, Thiopeptide antibiotics stimulate biofilm formation in Bacillus subtilis. *Proc Natl Acad Sci U S A* **112**, 3086-3091 (2015).
27. K. Drescher, Carey D. Nadell, Howard A. Stone, Ned S. Wingreen, Bonnie L. Bassler, Solutions to the Public Goods Dilemma in Bacterial Biofilms. *Current Biology* **24**, 50-55 (2014).
28. D. Romero, C. Aguilar, R. Losick, R. Kolter, Amyloid fibers provide structural integrity to Bacillus subtilis biofilms. *Proceedings of the National Academy of Sciences* **107**, 2230-2234 (2010).
29. D. Romero, H. Vlamakis, R. Losick, R. Kolter, Functional Analysis of the Accessory Protein TapA in Bacillus subtilis Amyloid Fiber Assembly. *Journal of Bacteriology* **196**, 1505-1513 (2014).
30. L. Chai, D. Romero, C. Kayatekin, B. Akabayov, H. Vlamakis, R. Losick, R. Kolter, Isolation, characterization, and aggregation of a structured bacterial matrix precursor. *Journal of Biological Chemistry* **288**, 17559-17568 (2013).
31. N. El Mammeri, J. Hierrezuelo, J. Tolchard, J. Camara-Almiron, J. Caro-Astorga, A. Alvarez-Mena, A. Dutour, M. Berbon, J. Shenoy, E. Morvan, A. Grelard, B. Kauffmann, S. Lecomte, A. de Vicente, B. Habenstein, D. Romero, A. Loquet, Molecular architecture of bacterial amyloids in Bacillus biofilms. *FASEB J*, fj201900831R (2019).
32. I. Dogsa, M. Brloznik, D. Stopar, I. Mandic-Mulec, Exopolymer diversity and the role of levan in Bacillus subtilis biofilms. *PLoS One* **8**, e62044 (2013).
33. A. Dragoš, H. Kiesewalter, M. Martin, C.-Y. Hsu, R. Hartmann, T. Wechsler, C. Eriksen, S. Brix, K. Drescher, N. Stanley-Wall, R. Kümmerli, Á. T. Kovács, Division of Labor during Biofilm Matrix Production. *Current Biology* **28**, 1903-1913.e1905 (2018).

34. S. B. Otto, M. Martin, D. Schäfer, R. Hartmann, K. Drescher, S. Brix, A. Dragoš, T. Kovács Á, Privatization of Biofilm Matrix in Structurally Heterogeneous Biofilms. *mSystems* **5**, (2020).
35. C. D. Nadell, K. Drescher, N. S. Wingreen, B. L. Bassler, Extracellular matrix structure governs invasion resistance in bacterial biofilms. *The ISME Journal* **9**, 1700-1709 (2015).
36. X. Qiu, P. Setlow, Structural and Genetic Analysis of X-Ray Scattering by Spores of Bacillus subtilis. *Journal of Bacteriology* **191**, 7620-7622 (2009).
37. J. N. Wilking, V. Zaburdaev, M. De Volder, R. Losick, M. P. Brenner, D. A. Weitz, Liquid transport facilitated by channels in Bacillus subtilis biofilms. *Proceedings of the National Academy of Sciences* **110**, 848 (2013).
38. N. S. Jakubovics, R. C. Shields, N. Rajarajan, J. G. Burgess, Life after death: the critical role of extracellular DNA in microbial biofilms. *Letters in applied microbiology* **57**, 467-475 (2013).
39. X. Zuo, G. Cui, K. M. Merz, L. Zhang, F. D. Lewis, D. M. Tiede, X-ray diffraction "fingerprinting" of DNA structure in solution for quantitative evaluation of molecular dynamics simulation. *Proceedings of the National Academy of Sciences of the United States of America* **103**, 3534 (2006).
40. T. Phan-Xuan, E. Bogdanova, A. Millqvist Fureby, J. Fransson, A. E. Terry, V. Kocherbitov, Hydration-Induced Structural Changes in the Solid State of Protein: A SAXS/WAXS Study on Lysozyme. *Molecular Pharmaceutics* **17**, 3246-3258 (2020).
41. L. B. Skinner, C. Huang, D. Schlesinger, L. G. M. Pettersson, A. Nilsson, C. J. Benmore, Benchmark oxygen-oxygen pair-distribution function of ambient water from x-ray diffraction measurements with a wide Q-range. *The Journal of Chemical Physics* **138**, 074506 (2013).
42. M. Bodík, D. Krajčíková, J. Hagara, E. Majkova, I. Barák, P. Šiffalovič, Diffraction pattern of Bacillus subtilis CotY spore coat protein 2D crystals. *Colloids and surfaces. B, Biointerfaces* **197**, 111425 (2021).
43. H. Kadota, K. Iijima, The X-ray Diffraction Pattern of Spores of Bacillus subtilis. *Agricultural and Biological Chemistry* **29**, 80-81 (1965).
44. J. H. Scofield, Relativistic hartree-slater values for K and L X-ray emission rates. *Atomic Data and Nuclear Data Tables* **14**, 121-137 (1974).
45. J. H. Scofield, "Theoretical photoionization cross sections from 1 to 1500 keV" (UCRL--51326, 1973; http://inis.iaea.org/search/search.aspx?orig_q=RN:05099181).
46. P. Onder, A. Tursucu, D. Demir, K Shell X-Ray Fluorescence Parameters of Some Elements in the Atomic Range. *Science and Technology of Nuclear Installations* **2013**, 285190 (2013).
47. M. O. Krause, Atomic radiative and radiationless yields for K and L shells. *Journal of Physical and Chemical Reference Data* **8**, 307-327 (1979).
48. M.-K. Kwak, H.-B. Ryu, S.-H. Song, J.-W. Lee, S.-O. Kang, Anti-σ factor YlaD regulates transcriptional activity of σ factor YlaC and sporulation via manganese-dependent redox-sensing molecular switch in Bacillus subtilis. *Biochemical Journal* **475**, 2127-2151 (2018).
49. P. Y. Chung, R. Khanum, Antimicrobial peptides as potential anti-biofilm agents against multidrug-resistant bacteria. *Journal of Microbiology, Immunology and Infection* **50**, 405-410 (2017).
50. M. Nishikawa, K. Kobayashi, M. Henkin Tina, Calcium Prevents Biofilm Dispersion in Bacillus subtilis. *Journal of Bacteriology* **203**, e00114-00121.
51. A. Diehl, Y. Roske, L. Ball, A. Chowdhury, M. Hiller, N. Moliere, R. Kramer, D. Stoppler, C. L. Worth, B. Schlegel, M. Leidert, N. Cremer, N. Erdmann, D. Lopez, H. Stephanowitz, E. Krause, B. J. van Rossum, P. Schmieder, U. Heinemann, K. Turgay, U. Akbey, H. Oschkinat, Structural changes of TasA in biofilm formation of Bacillus subtilis. *Proc Natl Acad Sci U S A* **115**, 3237-3242 (2018).
52. E. Erskine, R. J. Morris, M. Schor, C. Earl, R. M. C. Gillespie, K. M. Bromley, T. Sukhodub, L. Clark, P. K. Fyfe, L. C. Serpell, N. R. Stanley-Wall, C. E. MacPhee, Formation of functional, non-amyloidogenic fibres by recombinant Bacillus subtilis TasA. *Mol Microbiol* **110**, 897-913 (2018).

53. D. N. Azulay, M. Ghrayeb, I. B. Ktorza, I. Nir, R. Nasser, Y. S. Harel, L. Chai, Colloidal-like aggregation of a functional amyloid protein. *Physical Chemistry Chemical Physics* **22**, 23286-23294 (2020).
54. M. Ghrayeb, S. Hayet, N. Lester-Zer, Y. Levi-Kalisman, L. Chai, Fibrilar Polymorphism of the Bacterial Extracellular Matrix Protein TasA. *Microorganisms* **9**, 529 (2021).
55. B. Li, P. Ge, K. A. Murray, P. Sheth, M. Zhang, G. Nair, M. R. Sawaya, W. S. Shin, D. R. Boyer, S. Ye, D. S. Eisenberg, Z. H. Zhou, L. Jiang, Cryo-EM of full-length α-synuclein reveals fibril polymorphs with a common structural kernel. *Nature Communications* **9**, 3609 (2018).
56. R. Nelson, M. R. Sawaya, M. Balbirnie, A. O. Madsen, C. Riekel, R. Grothe, D. Eisenberg, Structure of the cross-[beta] spine of amyloid-like fibrils. *Nature* **435**, 773-778 (2005).
57. M. R. Sawaya, S. Sambashivan, R. Nelson, M. I. Ivanova, S. A. Sievers, M. I. Apostol, M. J. Thompson, M. Balbirnie, J. J. W. Wiltzius, H. T. McFarlane, A. O. Madsen, C. Riekel, D. Eisenberg, Atomic structures of amyloid cross-[bgr] spines reveal varied steric zippers. *Nature* **447**, 453-457 (2007).
58. L. Goldschmidt, P. K. Teng, R. Riek, D. Eisenberg, Identifying the amylome, proteins capable of forming amyloid-like fibrils. *Proceedings of the National Academy of Sciences* **107**, 3487-3492 (2010).
59. G. Benecke, W. Wagermaier, C. Li, M. Schwartzkopf, G. Flucke, R. Hoerth, I. Zizak, M. Burghammer, E. Metwalli, P. Müller-Buschbaum, M. Trebbin, S. Förster, O. Paris, S. V. Roth, P. Fratzl, A customizable software for fast reduction and analysis of large X-ray scattering data sets: applications of the new DPDAK package to small-angle X-ray scattering and grazing-incidence small-angle X-ray scattering. *Journal of applied crystallography* **47**, 1797-1803 (2014).
60. J. Schindelin, I. Arganda-Carreras, E. Frise, V. Kaynig, M. Longair, T. Pietzsch, S. Preibisch, C. Rueden, S. Saalfeld, B. Schmid, J.-Y. Tinevez, D. J. White, V. Hartenstein, K. Eliceiri, P. Tomancak, A. Cardona, Fiji: an open-source platform for biological-image analysis. *Nature Methods* **9**, 676-682 (2012).